Variable Geometry Cochlear Model at Low Input Frequencies: A Basis for Compensating Morphological Disorders

Abstract: The implementation of an algorithm suitable for interactive experimentation with a mathematical model of the cochlea is described. In the model, the cochlea's exterior shell is represented by a surface of revolution. Internally, the cochlea is partitioned symmetrically into two chambers (the scalae) by a midplane representing the basilar membrane with its bony supports together with the "collapsed" cochlear duct (third chamber). The two chambers are filled with a viscous and incompressible fluid and communicate through a small opening (the helicotrema), at the cochlea's apex. The system is driven by the piston-like movement with frequency ω of the stapes at the cochlea's basal end. An isotropic sectorial plate widening toward the apex represents the basilar membrane. Some of the effects of the cochlear duct are considered through a provision for nonzero net pressure at the basilar membrane's apical end. The behavior of this system in the neighborhood of the low-frequency threshold, where the effects of cochlear geometry are most pronounced, is described from the solutions of the equations of motion for $\omega \rightarrow 0$.

Preface

From a mathematical model of the cochlea, whose formulation and solution are reported elsewhere, a research tool for cochlear mechanics has been developed. This application is reported here because it involves, among other things, considerable interactive graphics and computing.

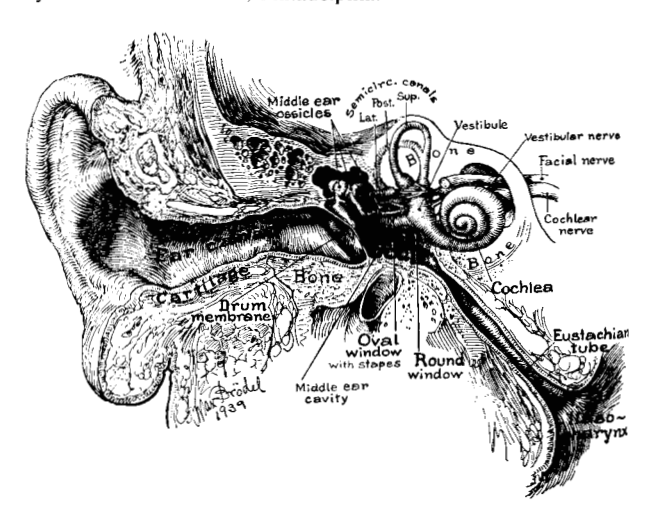
The user may specify any surface of revolution for the cochlea's exterior shell. Internally the cochlea is modeled as two- or three-chambered. The basilar membrane is represented by a tapered elastic plate. A variety of boundary conditions at the helicotrema may be optionally used. The behavior (i.e., place principle) of the model for input frequencies very close to the low-frequency threshold is computed and displayed. In this way pathologies that some researchers have partially attributed to abnormal variations in the shape of the cochlea can be studied. Also, insights into some optimal features of the cochlea's normal shape can be obtained.

Introduction

The ear is conveniently subdivided into three parts: outer, middle, and inner ear (Fig. 1). The outer ear consists of the external flap and the ear canal leading to the drum (i.e., tympanic) membrane of the middle ear. Attached to this membrane is a chain of three small bones called the middle ear ossicles. The innermost ossicle, called the stapes, has its footplate implanted at the oval window of the inner ear.

The auditory portion of the inner ear is a snail-shaped structure called the cochlea. With the exception of an initial bulge at the basal end, where the stapes is embedded, the cochlea narrows gradually towards its apex (apical end). In man it winds about 2.75 turns; its uncoiled length is about 35 mm. The cochlea (Fig. 2) is composed of three fluid-filled chambers (scala tympani, scala vestibuli, and scala media). The sense organ proper, i.e., the organ of Corti with its accessory structures,

Figure 1 Schematic of the ear, with the cochlea rotated somewhat from the normal orientation to show its coils more clearly. Reprinted with permission from *Unpublished Drawings of the Anatomy of the Human Ear*, by Max Brodel; copyright 1946 by W. B. Saunders Co., Philadelphia.



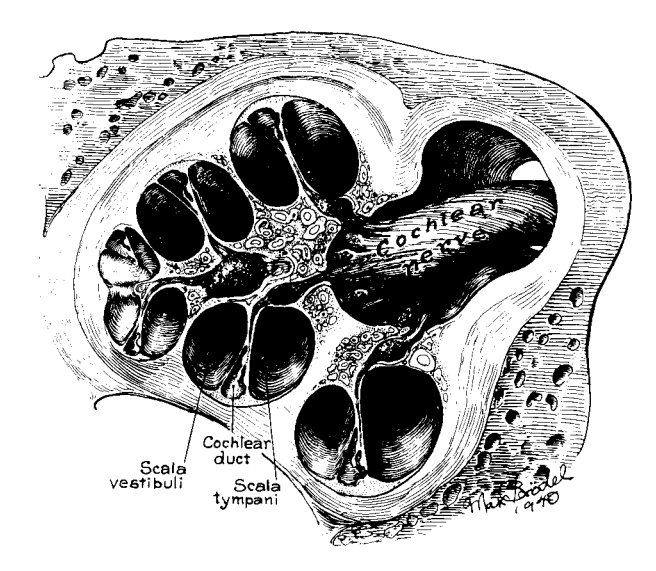


Figure 2 Cochlear cross section. Reprinted with permission from *The 1940 Year Book of Eye, Ear, Nose and Throat*, L. Bothman and S. J. Crowe, eds.; copyright 1940, Year Book Medical Publishers, Inc., Chicago.

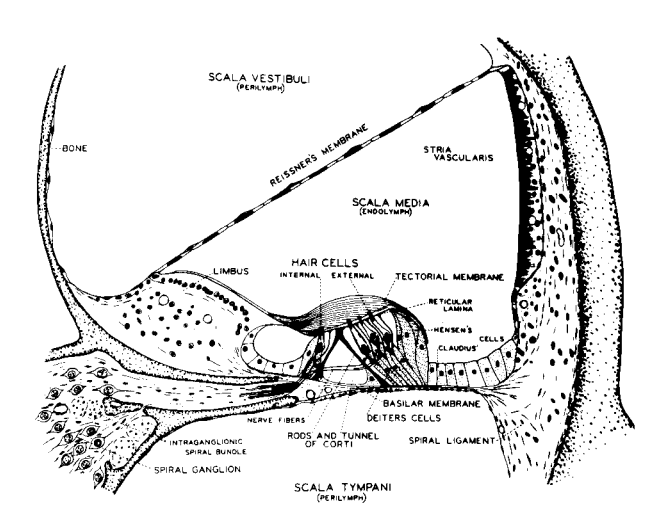


Figure 3 Cross section of the cochlear duct. Reprinted with permission from "Acoustic Trauma in the Guinea Pig," H. Davis et al., J. Acoust. Soc. Amer 25, 1180 (1953).

is contained in the scala media (also called the cochlear duct), and is supported by the fibrous basilar membrane that forms part of one wall of the cochlear duct (Fig. 3). The thin and pliant Reissner's membrane separates the cochlear duct from the scala vestibuli, which, at the basal end of the cochlea, communicates with the middle ear through the oval window. The scala tympani ends at the round window, an opening on the cochlear wall

covered by a membrane. The cochlear duct, formed by the basilar membrane and its supports and Reissner's membrane, ends "blindly" just short of the cochlear apex, leaving a small opening called the helicotrema. This opening allows the scala tympani to communicte with the scala vestibuli (see Figs. 4 and 5). The sensory surface of the spiral cochlea, then, is contained in the cochlear duct, a relatively narrow fluid-filled tube separating two communicating fluid-filled chambers.

Hearing results from two kinds of processes, one mechanical and the other electrochemical. The sound signal is conducted via the outer and middle ear to the cochlear fluids, which in turn force the basilar membrane to oscillate. These are the mechanical events in the auditory process (Fig. 6) [1-3]. While the conductive mechanism is relatively well understood, the manifestation of acoustical information in terms of the motion of the basilar membrane is not. Direct experimental measurements of cochlear function are difficult to obtain due to the inaccessibility of the cochlea and the delicate structure of the basilar membrane. Consequently, modeling is a particularly useful tool, and many mechanical, electrical, and mathematical cochlear models [4-21] have been developed. Surveys of cochlear modeling are given in [22] and [23].

Von Békesy [24] (for more recent data see [25-27] and also discussion in [22]) obtained extensive data on the cochlea and found that

- 1. The basilar membrane has neither longitudinal nor transverse tension in the resting state.
- 2. The stiffness of the basilar membrane decreases by about two orders of magnitude from the stapes to the helicotrema; the tapered shape of the membrane can account for this. The basilar membrane exhibits uniform elastic properties throughout (i.e., it is isotropic). However, Novoselova [16] has recently proposed that the basilar membrane is anisotropic.
- The damping of basilar membrane motion due to the cochlear fluid is essentially constant at all points on the membrane except near the helicotrema, where it increases.
- Traveling waves exist in the motion of the basilar membrane for excitation frequencies above 25 Hz.
- 5. There is a place principle—i.e., there exists a one-to-one correspondence between excitation frequencies and the positions of maximum membrane displacement. Low frequencies result in maxima close to the helicotrema and high frequencies produce maxima near the stapes (see Fig. 7).

The generally accepted modern version of the place principle is that there is no precise specificity of tonal action [1]. In fact, other secondary or even primary

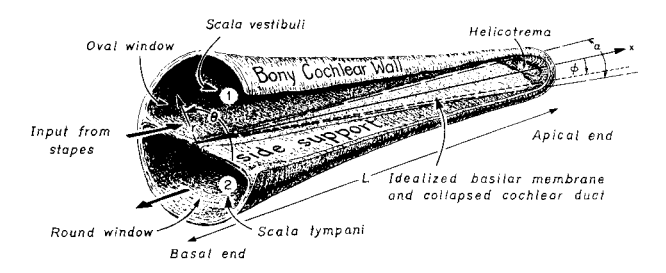


Figure 4 Three-dimensional two-chambered cochlear model.

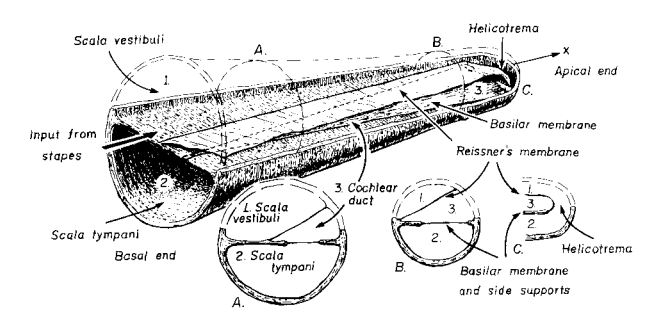


Figure 5 Three-chambered uncoiled cochlea. It differs from Fig. 4 in that it contains an additional narrow asymmetrical middle chamber ending "blindly" at the helicotrema.

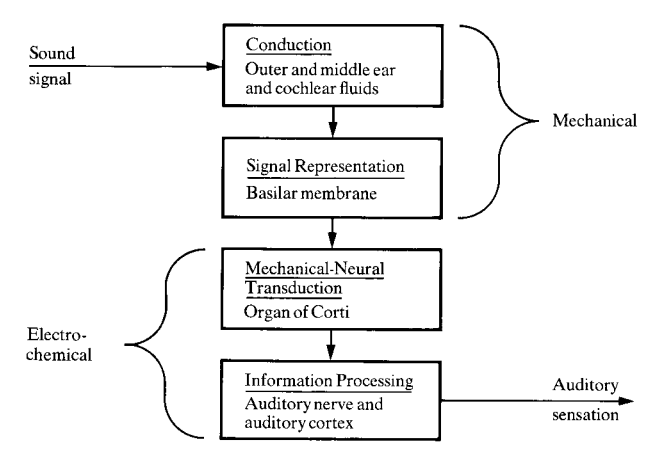


Figure 6 Sequence of auditory events.

mechanical and/or neural mechanisms for frequency analysis have been conjectured [28-30]. Nevertheless the place principle, because it is a mathematically precise and concise statement, often serves as a natural (and satisfactory) criterion for judging the efficacy of mathematical models of cochlear mechanics.

A recent two-dimensional uniform geometry cochlear model [19, 20] provides good qualitative agreement with the place principle at high frequencies. It shows

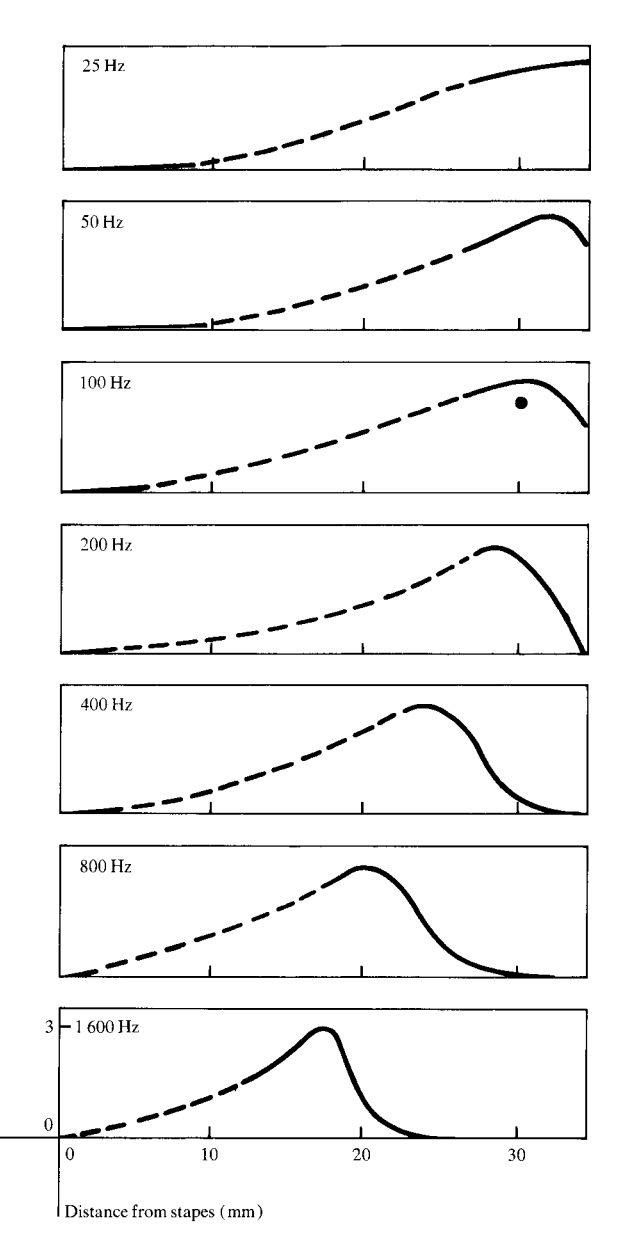


Figure 7 The place principle at low frequencies. The maximum of the time-envelope of the basilar membrane's oscillations shifts towards the stapes (basal end) with increasing frequency. Data obtained by G. von Békésy [24] from a cadaver specimen. Solid portions indicate measurements and dotted portions of the curves are interpolations.

Relative amplitude

that the high-frequency threshold is determined primarily by the mechanical properties of the cochlear fluids (i.e., viscosity and density) as well as by the modulus of elasticity E of the basilar membrane. For an isotropic basilar membrane it was conjectured that the low-frequency threshold is intimately related to the geometric structure of the cochlea including the basilar membrane's taper. This was confirmed with the formulation and study at low frequencies of a three-dimensional cochlear model

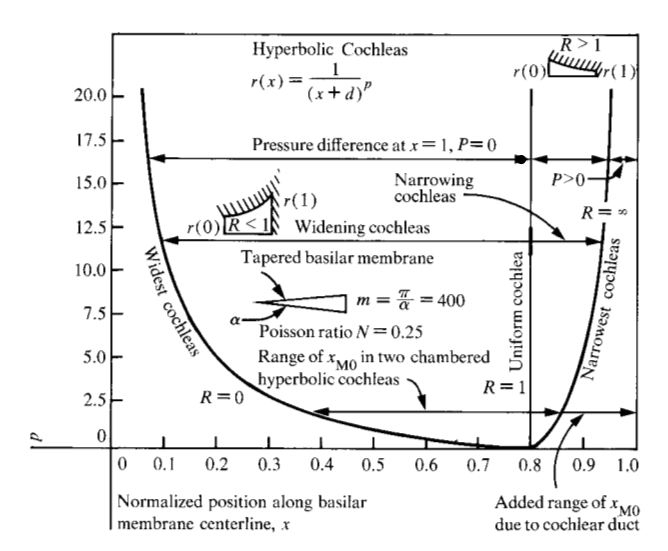


Figure 8 Summary of results for hyperbolic cochleas. Range of x_{M0} between curve for narrowest cochleas and x = 1 corresponds to quasi-three-chambered models.

endowed with some of the intricate geometry of the cochlea [21]. The stagewise evolution of this model is described in [22].

Here we exploit the general results in [21] and [22] to study quantitatively the relationship between the geometric structure of the cochlea and the low-frequency response at the basilar membrane level. First, we give a summary description of the model and the results obtained in [21] for a special class of cochlear shapes (see Fig. 8). Subsequently, by means of spline interpolation, arbitrary cochlear surfaces are constructed. The induced load on the basilar membrane at low input frequencies (idealized by $\omega \to 0$ where ω is the input frequency) is computed together with the resulting deformation of the basilar membrane's centerline. The computation can be carried out interactively, which makes it suitable for experimentation with the model.

Model

• Description

The geometry of the cochlea's main structures, as given here, is an idealization based on the data of Wever [31]. As in previous models, the cochlea is modeled uncoiled and consisting initially of two rather than three (actual) chambers. The external shape of the uncoiled cochlea (heretofore referred to as "shell") is well approximated by a conical surface of revolution with radius r(x) (Fig. 4). Because it is so thin, Reissner's membrane can transmit normal pressure from the scala vestibuli through the cochlear duct to the basilar membrane (Fig. 3). However, any shear waves that may form on its upper surface as a consequence of its interaction with the fluid of the

scala vestibuli will be attenuated by the contents of the cochlear duct before reaching the upper surface of the basilar membrane. Hence, Reissner's membrane and the gel-like fluid contents of the cochlear duct are represented by an idealized surface (capable of transmitting normal pressure, but not shear) contiguous to the upper surface of the basilar membrane. Further, it is assumed that no relative motion exists between the basilar membrane and this idealized surface. Internally, a plane consisting of the basilar membrane with its rigid supports divides the cochlea into two fluid-filled chambers (the scalae tympani and vestibuli). The midplane includes the idealized surface consisting of the Reissner's membrane and the collapsed cochlear duct. The width w(x) of the basilar membrane increases linearly as the cochlear cross section narrows. It is convenient to represent the basilar membrane as a circular sector of constant thickness, having a small opening angle α at the basal end (dotted lines in Fig. 4). Since the low-frequency effects are concentrated at the apical end, the small nonzero width of the basilar membrane at x = 0 can be safely neglected. Along the edges, $\phi = \pm \alpha/2$, the basilar membrane merges with the bony cochlear walls and is assumed to be supported by fixed hinges (in the parlance of elasticity theory this condition is often referred to as "simple supports"). Boundary conditions at x = L are discussed separately. The system is driven by the piston-like movement, with frequency ω , of the stapes anchored at the oval window, and the fluid passes through the helicotrema connecting the two chambers.

The mathematical description of the motion of such a system requires the three-dimensional Navier-Stokes and continuity equations for viscous and incompressible fluids. The deflections of the two-dimensional basilar membrane are described by the plate equation. Finding the simultaneous solutions of these partial differential equations for the appropriate initial and boundary conditions is, to put it mildly, a formidable task. Some observations concerning the motion of the system can be utilized to make a number of judicious simplifications.

Solution

Due to symmetry, the maximum deflection of the basilar membrane occurs along its centerline. To study the place principle, it is thus sufficient to know the basilar membrane's centerline (BMC) deflection. Further, as $\omega \to 0$, the time dependence is eliminated from the equations of motion and their solutions are readily obtained. This is shown in [21] and more concisely in [22]. The induced load $p_0(x)$ on the BMC is given by

$$p_0(x) = S_0 \left[1 - (1 - P) \frac{G(x)}{G(1)} \right], \tag{1}$$

where from this point on x (i.e., $x \to x/L$) is the normal-

ized distance along the cochlear axis from the base to apex, and S_0 is the amplitude of the stapes' oscillation at x = 0. The constant $0 \le P < 1$ represents a possible pressure difference at the BMC's apical end (x = 1, discussed later in greater detail), and

$$G(x) = \int_{a}^{x} \frac{ds}{r^{3}(s)}.$$

Note that the load $p_0(x)$ is provided for an arbitrary cochlear radius $r(x) \neq 0$ and that $p_0(x)$ is strictly monotone decreasing and is bounded by $PS_0 \leq p_0(x) \leq S_0$.

The sectorial plate, representing the basilar membrane, has thickness d, modulus of elasticity E and Poisson ratio N, all assumed constant. The BMC deflection $a_0(x)$ is conveniently expressed by

$$a_0(x) = Ax^m + Cx^{m+2} + a_{0_n}(x), (2)$$

where the constants A and C are determined from the boundary conditions at x = 1, $m = \pi/\alpha$, with $\alpha \approx 8 \times 10^{-3}$ radians being the opening angle of the sectorial plate, and

$$a_{0_n}(x) = A(x)x^m + C(x)x^{m+2},$$
(3)

$$A(x) = \int_0^x \frac{1}{x_4^{2m+1}} \left[\int_0^{x_4} x_3^{2m} H(x_3) dx_3 \right] dx_4, \tag{3a}$$

$$C(x) = \int_0^x \frac{1}{x_2^{2m+1}} \left[\int_0^{x_2} x_1^{2m} R(x_1) dx_1 \right] dx_2, \tag{3b}$$

where

$$R(x) = \frac{p_0(x)}{2D(m+1)x^{m-1}}, \qquad D = \frac{Ed^3}{12(1-N^2)}, \text{ and}$$

$$H(x) = -x^{2}R(x) - \frac{4}{x^{2m-1}} \int_{0}^{x} x_{1}^{2m}R(x_{1}) dx_{1}.$$

· Boundary conditions at the helicotrema

At the apical end, three kinds of end supports - hingedend, free-end, and elastic-end-are investigated. All these constraints are expressed as particular cases (i.e., specifying the c_{ij}) of the two independent linear com-

$$\begin{cases} c_{11}a_0(1) + c_{12}a_0'(1) + c_{13}a_0''(1) + c_{14}a_0'''(1) = 0, \text{ and} \\ c_{21}a_0(1) + c_{22}a_0'(1) + c_{23}a_0''(1) + c_{24}a_0'''(1) = 0. \end{cases}$$
(4)

For example, if the edge at x = 1 is simply supported (hinged), (4) becomes

$$\begin{cases} a_0(1) = 0, \\ a_0''(1) + Na_0'(1) = 0, \end{cases}$$

$$A_{\rm h} = \frac{-(m+2)(m+1+N)a_{0_p}(1) + Na_{0_p}'(1) + a_{0_p}''(1)}{2(2m+1+N)}, \qquad A_{\rm E} = \frac{e_{\rm E}m(m+2M_{\rm E}) - E_{\rm E}(m+2N_{\rm E})}{m(m-1)(1-N)Q}, \text{ and } A_{\rm E} = \frac{e_{\rm E}m(m+2M_{\rm E}) - E_{\rm E}(m+2N_{\rm E})}{m(m-1)(1-N)Q}$$

$$C_{\rm h} = \frac{m(m-1+N) \, a_{0_p}(1) - N a_{0_p}'(1) - a_{0_p}''(1)}{2(2m+1+N)},$$

for the two constants in (2) with the subscript h indicating the hinged-end condition.

When the edge at x = 1 is unconstrained (the free-end condition, subscripted by f), (4) becomes

$$\begin{cases} a_0''(1) + N[a_0'(1) - m^2 a_0(1)] = 0, \\ a_0'''(1) + (2 - N)[a_0''(1) - (1 + m^2)a_0'(1) + 2m^2 a_0(1)] = 0, \end{cases}$$

and upon substitution from (2), provides the coefficients

$$A_{\rm f} = \frac{E_{\rm f}(m+2N_{\rm f}) - e_{\rm f}m(m+2M_{\rm f})}{2m(m-1)(m-2P_{\rm e})(3+N)}$$

$$C_{\rm f} = \frac{e_{\rm f}(m-2) - E_{\rm f}}{2(m+1)(m-2P_{\rm f})(3+N)},$$

$$N_{\rm f} = \frac{1+N}{1-N}, \qquad M_{\rm f} = -\frac{3-N}{1-N}, \qquad P_{\rm f} = \frac{1+N}{3+N},$$

$$\begin{split} E_{\rm f} &= a_{0_p}^{\prime\prime\prime}(1) + (2-N) \\ &\times \big[a_{0_p}^{\prime\prime}(1) - (1+m^2) a_{0_p}^{\prime}(1) + 2m^2 a_{0_p}(1) \big], \end{split}$$

$$e_{\rm f} = - \, a_{0_p}''(1) - N a_{0_p}'(1) + N m^2 a_{0_p}(1).$$

Finally we consider the elastic-end condition, where the edge at x = 1 functions as a narrow beam partially constraining the translation (with flexural rigidity B) and rotation (with torsional rigidity C') of the basilar membrane there. In this case, (4) is

$$\begin{cases} -m^2(N+2a)a_0(1) + [(m^2+1)a+N]a_0'(1) \\ + (1-a)a_0''(1) = 0, \end{cases}$$
and
$$[2m^2(2-N) - m^2b(8+m^2)]a_0(1) \\ + [-(2-N)(m^2+1) + 3b(2m^2+1)]a_0'(1) \\ + (2-N-3b)a_0''(1) + a_0'''(1) = 0, \end{cases}$$

where
$$a = -C'/D$$
 and $b = B/D$.

When a = b = 0, the end beam offers no constraints, so these equations reduce to the free-end condition as a special case.

Solving for A and C and subscripting by E gives

$$A_{\rm E} = \frac{e_{\rm E} m (m + 2 M_{\rm E}) - E_{\rm E} (m + 2 N_{\rm E})}{m (m - 1) (1 - N) Q}$$
, and

$$C_{\rm E} = \frac{E_{\rm E} - e_{\rm E}(m-2)}{(m+1)(1-N)Q},$$

with

$$Q = m(m + 2M_{\rm E}) - (m - 2)(m + 2N_{\rm E}),$$

$$T = 1 + \frac{a(m-2)}{(1-N)}, \qquad N_{\scriptscriptstyle \rm E} = \frac{1+N}{T(1-N)},$$

$$P_{\rm E} = 1 + \frac{b(m-3)}{1-N}, \qquad M_{\rm E} = \frac{N-3-b(2m-3)}{1-N+b(m-3)},$$

$$E_{\rm E} = \frac{E_{\rm E_1}}{P}, \qquad e_{\rm E} = \frac{e_{\rm E_1}}{T},$$

$$\begin{split} e_{\rm E_1} &= - \, (1-a) \, a_{0_p}''(1) - [\, (m^2+1)a + N] \, a_{0_p}'(1) \\ &+ m^2 \, (N+2a) \, a_{0_p}(1) \, , \end{split}$$

and

$$\begin{split} E_{\rm E_1} &= a_{\rm 0_p}'''(1) + \big[(2-N) - 3b \big] a_{\rm 0_p}''(1) \\ &+ \big[-(2-N) \left(m^2 + 1 \right) + 3b (2m^2 + 1) \big] a_{\rm 0_p}'(1) \\ &+ \big[2m^2 (2-N) - m^2 b (8+m^2) \big] a_{\rm 0_p}'(1). \end{split}$$

We can now study the behavior of the model as $\omega \to 0$.

The elastic properties of the basilar membrane appear only in D [defined after (3)], which in turn appears in R(x). With (4) being homogeneous in $a_0^{(i)}(1)$, i=0,1,2,3, it is easily seen that in A and C, and hence $a_0(x)$, D occurs only in the factor 1/D throughout. Therefore, the position x_{M0} of the maximum of $a_0(x)$ is independent of the basilar membrane's elastic properties. We can conclude that the low-frequency threshold (i.e., place principle: location of x_{M0} as $\omega \to 0$) is determined only from the cochlear geometry [i.e., r(x)] and boundary conditions at x=1 (i.e., the constants A and C).

• Hyperbolic quasi-three-chambered cochlear model It was mentioned in the introduction that the efficacy of a cochlear model is, in general, judged with respect to the place principle. For the purpose of this discussion it suffices to consider the following properties of the place principle. For an input frequency ω , let $x_{\text{max}}(\omega)$ be the position, along the basilar membrane, where the maximum (for all time t) oscillation occurs. It is required that

 $x_{\text{max}}(\omega)$ be a continuous function with $x_{\text{max}} \downarrow \omega$,

$$\lim_{m \to \infty} x_{\text{max}} = 0 \qquad \text{(basal end), and} \tag{5}$$

$$x_{\text{Mo}} = \lim_{\omega \to 0} x_{\text{max}} = 1$$
 (apical end); (6)

(see Fig. 7).

Condition (5) pertains to the high-frequency threshold and is essentially due to the signal input at x = 0. To optimize, that is, to use the full length of the basilar membrane for frequency discrimination, nature put x_{M0} at x = 1 [condition (6)]. How is this done? Equation (1)

provides the crucial clue. It shows that as $\omega \to 0$, any symmetric cochlea induces a strictly monotone decreasing load $p_0(x)$ on the basilar membrane. The only way that the position of maximum deflection x_{M0} can approach x=1 for such a load is for a basilar membrane having a monotone decreasing stiffness; ergo: the widening taper of the basilar membrane.

The most convenient shapes to study using Eq. (1) are "hyperbolic cochleas" of the form

$$r(x) = \frac{1}{(x+d)^p}, \quad \text{for } p > 0.$$
 (7)

A natural way to determine d is by specifying the ratio R = r(0)/r(1), which measures the cochlea's narrowing ("taper"). In humans $R \approx 3$, and in the range $1/3 \le p \le 2$, Eq. (7) yields shapes resembling that of an uncoiled cochlea. These shapes were in fact studied extensively in [21], and the results of that study are summarized in Fig. 8. It was found that for each p,

$$\frac{4}{3p+5} \le x_{M0} \le \left(\frac{4}{3p+5}\right)^{1/(3p+1)},\tag{8}$$

this being independent of the boundary conditions at x=1. For narrowing cochleas, the $x_{\rm M0}$ is close to the upper bound, while for widening cochleas, $x_{\rm M0}$ approaches the lower bound. For R=1, that is, when the cochlea is uniform (cylindrical), $x_{\rm M0}=4/5$ [from (8) with p=0]. We conclude that the narrowing of the cochlea is desirable since it pushes $x_{\rm M0}$ toward x=1. However, for realistic values of p (say less than 2) and $R\approx 3$, the narrowing of the cochlea and the basilar membrane's widening taper are not sufficient to bring $x_{\rm M0}$ to 1 (i.e., $0.38 \le x_{\rm M0} \le 0.85$).

Let us look again at the human cochlea (particularly Fig. 2). Uncoiled, it looks somewhat like Fig. 5 with three chambers, rather than the two chambers we have considered so far. The middle chamber (cochlear duct) plays a crucial role at very low frequencies.

In two-chamber models the net pressure on the basilar membrane's apical end is the same as the net pressure at the adjacent helicotrema. There, with the possible exception of some slight friction losses, we have unimpeded fluid flow. Hence the pressures just above and below the helicotrema balance (pressure equalization). With three chambers, however, the net pressure [here called $p_{\text{net}}(1)$] along the edge x=1 of the basilar membrane is not zero, since the basilar membrane is shielded from the helicotrema by Reissner's membrane. Consequently, $p_{\text{net}}(1)$ is the difference between the pressures at x=1 (see detail C in Fig. 5) in the scala tympani and cochlear duct (rather than the scala vestibuli as is the case in two-chambered cochleas). A preliminary study of a three-chambered cochlea [32] showed that

$$p_{\rm net}(1) \approx 0.3 S_{\rm o}$$

where S_0 is the input pressure from the stapes at x = 0. For this reason the constant P is introduced in (1). We write

$$p_{\text{net}}(1) = PS_0$$

where P is a constant somewhat larger than 0.3 to allow for small friction losses in the fluid flow. With this condition the model may be called "quasi-three-chambered," since at least as $\omega \to 0$, it accounts for the effects of the cochlear duct. We will see that in quasi-three-chambered cochleas, $x_{\rm M0}$ comes close to x=1 (Fig. 8), and the boundary conditions there influence $x_{\rm M0}$. As long as $x_{\rm M0}$ is far from x=1 (say $x_{\rm M0} \le 0.92$), the constraints there do not affect it.

Cochleas whose shells are arbitrary surfaces of revolution

Physiologically, the lower frequencies are particularly important since they dominate in speech (e.g., only frequencies up to about 2 kHz are reliably transmitted over the telephone). We have seen that cochlear geometry influences primarily the low-frequency response. So far, for mathematical convenience, only hyperbolic shells have been studied. However, the generality of (1) permits the study of cochleas enclosed by an arbitrary surface of revolution. The microstructure at the basilar membrane's apical end (boundary conditions at x = 1) may be examined as well. In this way the cochlea's normal shape, as we will see in the next section, can be better understood.

There are also clinical motivations. Several hearing pathologies such as cochlear otosclerosis and otospongiosis, endolymphatic hydrops (Ménière's disease), and others (see Table 1) have been morphologically linked with anomalous variations in the cochlea's internal geometry. These variations take the form of hardening or protrusions of the cochlear walls, distension of the cochlear duct through the displacement of Reissner's membrane, atrophy or rupturing of the basilar membrane, etc. To what extent can pathological behavior be attributed to shape deformations? By imitating such shape variations in the cochlear model we can better assess the relationship between the pathology (i.e., deficiencies in perceiving low-frequency sounds) and the associated anomalous shapes.

While it is nearly impossible to intrude into the interior of the cochlea without destroying it, it is relatively easy to reach the external cochlear shell. Perhaps the function of a cochlea having internal defects can be restored to normal (or can at least be improved) by making small compensating alterations in the shape of the cochlear shell. This clinically exciting prospect as well as the other points outlined above can be explored with the computational cochlear model described in this section.

Table 1 Some disorders affecting the morphology of the cochlea (compiled from Reference [33]).

- I. Affected region: osseous labyrinth (cochlear portion)
 - A. Formation or destruction of bone on labyrinth walls
 1. Bone diseases
 - a. Otosclerosis: Spongy bone may form in the cochlea, particularly near the oval and round windows.
 Otosclerosis causes deafness in more than one percent of the population.
 - b. Paget's disease: In the cochlea this disease causes active reconstruction of bone. Two symptoms differing from those of otosclerosis are tinnitus and rapid loss of hearing.
 - c. Osteogenesis imperfecta: A general symptom is fragility of bones. In the cochlea, growth of spongy bone may be hard to distinguish from otosclerosis.
 - Purulent labyrinthitis: Lining of the cochlea is inflamed and bone formation may be stimulated. This may be associated with inflammation of the middle ear (otitis media) or with cerebrospinal meningitis.
 - Syphilis: Bone growth and destruction may result in a variety of deformations. Deafness occurs rather suddenly with symptoms like those of Ménière's disease.
 - Cogan's syndrome: Bone formation, often in the scala media, distinguishes this from Ménière's disease. Symptoms are like those of Ménière's disease.
 - Pendred's syndrome: Associated with goiter, this disorder may result in hydrops (see Ménière's disease) and in incomplete development of or bone growths in the labyrinth.
 - B. Miscellaneous effects
 - 1. Genetic deformities.
 - 2. Fractures of the temporal bone.
- II. Affected region: membranous labyrinth (cochlear portion)
 - A. Distension or collapse of Reissner's membrane
 - Ménière's disease: Excess endolymph builds up (endolymphatic hydrops) and causes Reissner's membrane to bulge (and occasionally rupture). Symptoms include deafness, vertigo and tinnitus.
 - Serious labyrinthitis: Lining of cochlea is inflamed. Membranous labyrinth is distended, but not as much or as uniformly as in Ménière's disease.
 - Rubella: Infection of fetus may result in distension or collapse of Reissner's membrane.
 - Tuberculous meningitis: Reissner's membrane may be distended.
 - 5. Presbycusis: Loss of hearing with old age may be associated with degeneration of the neural and vascular networks in the cochlea. Failure of the vascular stria may cause Reissner's membrane to collapse. (Degeneration of the basilar membrane and the spiral ligament may also play a role in presbycusis.)
 - B. Miscellaneous effects
 - 1. Genetic deformities.
 - Neoplasms: Schwannoma tumors in the internal auditory meatus may lead to degenerative changes in the membranous labyrinth, particularly in the basal turn.

We offer a challenge, and an opportunity, to clinicians to provide a list of pathologies unequivocally due to defects in the cochlear shell and affecting low-frequency hearing. By comparing the model's predictions for these pathologies with the known behavior (data), the basic model can be validated or invalidated.

• Cochlear shell definition and construction

The shell is generated by rotating a planar curve about the x axis. Cubic splines are a convenient way of representing the generatrix and are well suited for interactive computation.

A general method of surface definition developed by Dimsdale [34] is adapted. The specific algorithm of spline interpolation used here is given in [35], work which was motivated by the needs of this study. We briefly discuss the process.

The user defines the cochlear radius r(x) by specifying a number of points which are usually called knots, (x_i, r_i) , $i = 1, \dots, N'$, lying on the desired curve. Subsequently, by means of the interpolation algorithm from [35], the spline r(x) is constructed on [0, 1] so that

- 1. $r(x_i) = r_i$, that is, the spline passes through every knot;
- 2. on each interval $I_i = [x_i, x_{i+1}], r(x)$ is a cubic polynomial in x-that is, r(x) is piecewise cubic on [0, 1];
- 3. at each knot, r(x) has continuous second derivatives; i.e., $r(x) \in C^2(0, 1)$; and
- 4. r(x) is the curve which minimizes the strain energy of the deformation from among all curves passing through the knots: r(x) "behaves" like a real material having stiffness.

Typically, for anything but the most unusual shapes, five to seven knots suffice to specify the desired shape. If needed, provisions exist for introducing additional constraints on the spline, including vertical slopes at any given points. In that case the resulting spline has somewhat weaker properties than 1 through 4 (see [34] and [35]).

This process provides us with a specification

$$r_i(x) = b'_{0i}x^3 + b'_{1i}x^2 + b'_{2i}x + b'_{3i}$$
(9)

of the generatrix r(x) on I_i , $i = 1, \dots, N' - 1$. Note that since $r(x) \neq \forall x \in [0, 1]$ (that is, the cochlear passages are not blocked), $r_i(x) \neq 0$ on I_i .

• Evaluation of the load and BMC deflection The integral

$$G(x) = \int_0^x \frac{du}{r^3(u)}$$

occurring in the load $p_0(x)$ in Eq. (1) is calculated by expanding the integrand in a power series. An efficient scheme for obtaining the power series of the reciprocal of a polynomial (and in general of the reciprocal of an analytic function) is given in [36]. Specifically, if $p_k(z)$ is a polynomial of degree k in the complex variable z, then the coefficients of the reciprocal series

$$\frac{1}{p_k(z)} = \sum_{n=0}^{\infty} a_n z^n \tag{10}$$

can be found by means of the recursive formula

$$\sum_{j=0}^{k} (-1)^{n-j} b_j a_{n-j} = 0, \tag{11}$$

where

$$p_k(z) = \sum_{j=0}^k b_j z^j.$$

Alternatively, since (11) is a kth order difference equation with constant coefficients, the a_n can be obtained in closed form [36] in terms of the zeros of $p_k(z)$.

The intervals of convergence of the series in (10) are determined by the location of the zeros of $p_k(z)$.

The power series of $1/r_i^3$ should converge on I_i . To check for convergence, we need to consider two cases. We use the notation λ_s , s = 1, 2, 3 for the zeros of $r_i(x)$, and $c_i = (x_i + x_{i+1})/2$ for the midpoint of I_i .

Case $I |\lambda_s - c_i| > c_i \forall s \in \{1, 2, 3\}$. Then the power series of $1/r_i^3$ about c_i converges on all of I_i .

Case $2 \ni s \in \{1, 2, 3\} \ni |\lambda_s - c_i| \le c_i$. In this case λ_s must be a complex zero since, as noted earlier, all real zeros of $r_i(x)$ are not on I_i . For convenience let $\lambda_2 = \lambda_s$, $\lambda_3 = \bar{\lambda}_s$, and let λ_1 be the real zero of $r_i(x)$. We subdivide I_i into the subintervals $I_{i_1} = [x_i, Re(\lambda_s)]$ and $I_{i_2} = [Re(\lambda_s), x_{i+1}]$. Letting c_{i_1} and c_{i_2} be the midpoints of I_{i_1} and I_{i_2} , respectively, we can see that the power series of $1/r_i^3$ about c_{i_1} , l = 1, 2, will converge on I_{i_2} .

The subdivision of I_i , as required by case 2, is carried out whenever necessary and results in $N-1 \ge N'-1$ subintervals of [0, 1]. For notational convenience the subintervals are relabeled consecutively from 1 to N-1. As well, the interval endpoints are enumerated consecutively by x_i for $i=1,\dots,N$.

A piecewise redefinition of the spline [i.e., Eq. (9)] is required wherever I_i is partitioned due to case 2 above. Such a redefinition in general alters the shape (i.e., the graph of the spline), which is unacceptable here since we wish to study the behavior of a *fixed* cochlear shape, while the spline redefinition is needed only for computational convenience. The interpolation algorithm used here provides splines (even those having vertical slopes at some points) that are unaffected by this process (i.e., interval subdivision), and hence the cochlear shell shape is left unaltered. This pertains to the *partition invariant* property of the splines (see discussion in [35]).

On each I_i , $i = 1, \dots, N - 1$, the series

$$\frac{1}{r_i^3(x)} = \sum_{n=0}^{\infty} a_{ni} (x - c_i)^n, \tag{12}$$

about the midpoint c_i of I_i , converges on all of I_i .

From the identity

$$\sum_{j=0}^{k} b_{j} x^{j} \equiv \sum_{j=0}^{k} B_{j} (x - c)^{j},$$

we obtain the formula

$$B_{j} = \sum_{r=j}^{k} {r \choose j} b_{r} c^{r-j},$$

by means of which $r_i^3(x)$ can be converted to a polynomial in $(x-c_i)$. Then (11), and the other results in [36], can be used to obtain the coefficients of the series in (12).

The evaluation of G(x) is now straightforward. For $x \in I_i$,

$$G(x) = \sum_{i=0}^{j-1} \int_{x_i}^{x_{i+1}} \frac{du}{r_i^3(u)} + \int_{x_j}^x \frac{du}{r_i^3(u)}.$$

Letting $L_i = x_{i+1} - x_i$, we obtain

$$G(x) = G_j + \sum_{n=0}^{\infty} \frac{a_{nj}}{n+1} (x - c_j)^{n+1},$$
 (13)

where

$$G_{j} = \sum_{i=0}^{j-1} \sum_{p=0}^{\infty} \frac{a_{2p,i} L_{i}^{2p+1}}{(2p+1)2^{2p}} - \sum_{n=0}^{\infty} (-1)^{n+1} \frac{a_{nj} L_{j}^{n+1}}{(n+1)2^{n+1}}.$$

From (13),

$$G(1) = \sum_{i=0}^{N-1} \sum_{n=0}^{\infty} \frac{a_{2n,i} L_i^{2n+1}}{(2n+1)2^{2n}}.$$

The load $p_0(x)$ given by (1) can be evaluated. Since S_0 occurs as a factor throughout it will not affect the position of the maximum deflection x_{M0} , so we may set $S_0 = 1$. For the same reason we take D = 1 in $a_{0p}(x)$ given by (3), the formula for the particular solution of the BMC deflection.

Proceeding with the calculation, we obtain

$$A(x)x^{m} = -\frac{x^{4}}{2(m+1)} \left\{ \frac{(m+6)}{(m+2)(16-m^{2})} \left[1 - \frac{(1-P)}{G(1)} G_{j} \right] - \frac{(1-P)}{G(1)} \sum_{n=0}^{\infty} \frac{a_{nj}}{n+1} \sum_{r=0}^{n+1} {n+1 \choose r} (-c_{j})^{r} x^{n+1-r} \times \left[(m+n+3-r)(m+n+5-r)(-m+n+5-r) \right]^{-1} \right\},$$
(14a)

and

$$C(x)x^{m+2} = \frac{x^4}{2(m+1)} \left\{ \frac{1}{(4-m^2)} \left[1 - \frac{(1-P)}{G(1)} G_j \right] - \frac{(1-P)}{G(1)} \sum_{n=0}^{n+1} \frac{a_{nj}}{n+1} \sum_{n=0}^{n+1} \binom{n+1}{r} (-c_j)^r x^{n+1-r} \times \left[(m+n+3-r)(-m+n+3-r) \right]^{-1} \right\}.$$
 (14b)

Adding, we find that

$$a_{0p}(x) = -2x^{4} \left\{ \frac{1}{(m^{2} - 4)(m^{2} - 16)} \left[1 - \frac{(1 - P)}{G(1)} G_{j} \right] + \frac{(1 - P)}{G(1)} \sum_{n=0}^{\infty} \frac{a_{nj}}{(n+1)} \sum_{r=0}^{n+1} {n+1 \choose r} (-c_{j})^{r} x^{n+1-r} \right.$$

$$\times \left[(m+n+3-r)(-m+n+3-r) \right] \times (m+n+5-r)(-m+n+5-r) \right]^{-1} . \tag{15}$$

From (15) and the formulae following Eq. (4), the coefficients
$$A$$
 and C in (2) can be evaluated for the various boundary conditions. These coefficients together with

boundary conditions. These coefficients together with (15) provide the deflection $a_0(x)$ [see Eq. (2)] of the BMC as the input frequency $\omega \to 0$, for the cochlear geometry given by the spline $r_i(x)$ on I_i , $i = 1, \dots, N-1$.

We now estimate the errors arising in the computation of $p_0(x)$ and $a_0(x)$.

• Error bounds

The series in (12) for $1/r_i^3(x)$ converges uniformly on I_i . Hence for a given $\varepsilon > 0$, there is a minimum integer N_i such that the following inequality is true for all x in the interval I_i :

$$\left| \sum_{n=0}^{N_i} a_{ni} (x - c_i)^n - \frac{1}{r_i^3(x)} \right| < \frac{\varepsilon}{r_i^3(x)}.$$
 (16)

Since $r_i(x)$ is available, $1/r_i^3(x)$ can be computed directly and N_i can be explicitly found.

We let the superscript T stand for the variable (as indicated) computed from the truncated series. Specifically, let

$$G_i^T(x) = \sum_{n=0}^{N_i} a_{ni} \int_{x_i}^x (u - c_i)^n du$$

= $\sum_{n=0}^{N_i} \frac{a_{ni}}{n+1} [(x - c_i)^{n+1} - (x_i - c_i)^{n+1}].$

Then

$$|G_i^T(x) - G_i(x)| \le \int_{x_i}^x \left| \sum_{n=0}^{N_i} a_{ni} (u - c_i)^n - \frac{1}{r_i^3(u)} \right| du$$

$$< \varepsilon G_i(x). \tag{17}$$

For $x \in I_i$, write

$$G(x) = \sum_{i=0}^{j-1} G_i(x_{i+1}) + G_j(x),$$

and

$$G^{T}(x) = \sum_{i=0}^{j-1} G_{i}^{T}(x_{i+1}) + G_{j}^{T}(x),$$

so that

$$|G(x) - G^{T}(x)| \leq \sum_{i=0}^{j-1} |G_{i}(x_{i+1}) - G_{i}^{T}(x_{i+1})|$$

$$+ |G_{j}(x) - G_{j}^{T}(x)|$$

$$< \varepsilon \sum_{i=0}^{j-1} G_{i}(x) + \varepsilon G_{j}(x) = \varepsilon G(x).$$
 (18)

We have shown that the same relative error is incurred in the computation of G(x) as in the computation of $1/r^3(x)$. Proceeding with our estimates, we assume that $1 > \varepsilon > 0$. The inequalities

$$(1-\varepsilon)G(x) < G^{T}(x) < (1+\varepsilon)G(x),$$

obtained directly from (18), imply that $G^{T}(x) \ge 0$ since $G(x) \ge 0$. Specifically, for x = 1,

$$(1-\varepsilon)G(1) < G^{T}(1) < (1+\varepsilon)G(1).$$

Therefore,

$$\frac{1-\varepsilon}{1+\varepsilon}\frac{G(x)}{G(1)} < \frac{G^{T}(x)}{G^{T}(1)} < \frac{1+\varepsilon}{1-\varepsilon}\frac{G(x)}{G(1)},$$

so together with the identities

$$\frac{1+\varepsilon}{1-\varepsilon} = 1 + \frac{2\varepsilon}{1-\varepsilon}$$
 and

$$\frac{1-\varepsilon}{1+\varepsilon} = 1 - \frac{2\varepsilon}{1-\varepsilon},$$

we obtain

$$-\frac{2\varepsilon}{1+\varepsilon}\frac{G(x)}{G(1)} < \frac{G^{T}(x)}{G^{T}(1)} - \frac{G(x)}{G(1)} < \frac{2\varepsilon}{1-\varepsilon}\frac{G(x)}{G(1)}$$

In turn, this implies that

$$\left|\frac{G^{T}(x)}{G^{T}(1)} - \frac{G(x)}{G(1)}\right| < \frac{2\varepsilon}{1 - \varepsilon} \frac{G(x)}{G(1)},$$

since obviously $2\epsilon/(1-\epsilon) > 2\epsilon/(1+\epsilon)$.

Proceeding, we find that

$$|p_0(x) - p_0^T(x)| = (1 - P) \left| \frac{G(x)}{G(1)} - \frac{G^T(x)}{G^T(1)} \right|$$

$$< (1 - P) \frac{2\varepsilon}{1 - \varepsilon} \frac{G(x)}{G(1)}.$$
(19)

Since G(x)/G(1) is strictly monotone increasing while $p_0(x)$ is strictly monotone decreasing, controlling the relative error in the computation of $p_0(x)$ [more precisely $p_0^T(x)$] is a somewhat delicate matter.

When $P \neq 0$ (i.e., with the presence of a third chamber—the cochlear duct), the minimum value of $p_0(x)$ is $p_0(1) = P > 0$, and from (19) we have

$$|p_0(x) - p_0^T(x)| < \frac{2\varepsilon}{1 - \varepsilon} \frac{1 - P}{P} p_0(x), \quad P \neq 0.$$
 (20a)

When P = 0, however, a different consideration is needed.

Let $z_c = 10^{-m}$ be the "zero" of the computation. That is, if our computation is precise to within $10^{-(m-1)}$, then 10^{-m} and 0 are indistinguishable. Now the minimum $p_0(x)$ is $p_0(1) = 0$ (which we take as $p_0(1) = z_c$). Hence

$$|p_0(x) - p_0^T(x)| < \frac{2\varepsilon}{1 - \varepsilon} \frac{p_0(x)}{z_o}.$$

Actually, for $\varepsilon_1 = 2\varepsilon/z_{\rm c}(1-\varepsilon)$, we take $z_{\rm c} = 10^{-1}\varepsilon_1$ and obtain $\varepsilon_1 = \sqrt{20\varepsilon}$ for $\varepsilon \ll 1$. Therefore,

$$|p_0(x) - p_0^T(x)| < \sqrt{20\varepsilon} p_0(x), \quad \text{for } P = 0.$$
 (20b)

We combine the two cases and write

$$|p_0(x) - p_0^T(x)| < \varepsilon_1 p_0(x),$$
 (20c)

with ε_1 being given in (20a) or (20b).

Rewriting (20c) as

$$(1 - \varepsilon_1) p_0(x) < p_0^T(x) < (1 + \varepsilon_1) p_0(x),$$

we see that $p_0^T(x) \ge 0$, when $1 > \varepsilon_1 > 0$.

For the computed particular solution of the BMC deflection

$$a_{0_n}^T(x) = A^T(x)x^m + C^T(x)x^{m+2},$$

the bounds

$$(1 - \varepsilon_1) C(x) < C^T(x) < (1 + \varepsilon_1) C(x);$$

$$(1+\varepsilon_1)A(x) < A^T(x) < (1-\varepsilon_1)A(x)$$

are similarly obtained. Applied jointly, they imply that

$$|a_{\mathbf{0}_{p}}^{T}(x) - a_{\mathbf{0}_{p}}(x)| < \varepsilon_{1}|Q(x)|,$$
 (21)

where

$$Q(x) = C(x)x^{m+2} - A(x)x^{m}.$$

An estimate for Q(x) in terms of $a_{0p}(x)$ is needed. From (14a) and (14b) we find that

$$\begin{split} Q(x) &= -\frac{x^4}{(m+1)} \left\{ \left[\frac{m^3 + 4m^2 - 10m - 28}{(m+2)(16-m^2)(4-m^2)} \right] \left[1 - \frac{(1-P)}{G(1)} G_j \right] \right. \\ &\left. - \frac{(1-P)}{G(1)} \sum_{n=0}^{\infty} \frac{a_{nj}}{n+1} \sum_{r=0}^{n+1} \binom{n+1}{r} (-c_j)^r x^{n+1-r} \right. \\ &\left. \times \left[\frac{m^2 - n^2 - r^2 + 2nr + 2m - 10n + 10r + 23}{(m+n+3-r)(-m+n+3-r)(m+n+5-r)(-m+n+5-r)} \right] \right\}. \end{split}$$

We are actually interested in computing the BMC deflection for very small opening angles of the sectorial plate representing the basilar membrane. This is equivalent to m being large (for example, m = 400). For large m we can approximate and obtain

$$Q(x) \approx -\frac{x^4}{m} \left\{ \frac{1}{m^2} \left[1 - \frac{(1-P)}{G(1)} G_j \right] - \frac{(1-P)}{G(1)} \right.$$
$$\times \sum_{n=0}^{\infty} \frac{a_{nj}}{(n+1)} \sum_{r=0}^{n+1} \frac{\binom{n+1}{r} (-c_j)^r x^{n+1-r}}{(m+n-r)(-m+n-r)} \right\}.$$

Similarly, for large m we obtain from (15) that

$$\begin{split} a_{0p}(x) &\approx -2x^4 \left\{ \frac{1}{m^4} \left[1 - \frac{(1-P)}{G(1)} \; G_j \right] + \frac{(1-P)}{G(1)} \right. \\ &\times \sum_{n=0}^{\infty} \frac{a_{nj}}{n+1} \; \sum_{r=0}^{n+1} \frac{\binom{n+1}{r} (-c_j)^r x^{n+1-r}}{(m+n-r)^2 (-m+n-r)^2} \right\}. \end{split}$$

The contribution of the individual terms to the indicated sums becomes negligible well before n reaches the value of m = 400. By comparison to m, then, we can neglect n and r to obtain the approximations

$$\begin{split} Q(x) \approx & -\frac{x^4}{m^3} \bigg[1 - \frac{(1-P)}{G(1)} \, G_j + \frac{(1-P)}{G(1)} \\ & \times \sum_{n=0}^{\infty} \frac{a_{nj}}{n+1} \, (x-c_j)^{n+1} \bigg], \end{split}$$

and

$$\begin{split} a_{0_p}(x) \approx & -\frac{2x^4}{m^4} \bigg[1 - \frac{(1-P)}{G(1)} + \frac{(1-P)}{G(1)} \\ & \times \sum_{n=0}^{\infty} \frac{a_{nj}}{n+1} \left(x - c_j \right)^{n+1} \bigg]. \end{split}$$

In turn, we have shown that for large m,

$$Q(x) \approx \frac{m}{2} \, a_{0_p}(x),$$

a very useful estimate enabling us, by means of (21), to complete the overall estimation of the computational error and obtain

$$|a_{\mathbf{0}_{p}}^{T}(x) - a_{\mathbf{0}_{p}}(x)| < \frac{\varepsilon_{1}m}{2} |a_{\mathbf{0}_{p}}(x)|.$$
 (22)

The error estimates in (18), (20), and (22) are given in terms of the relative error bound ε in (16). The convergence of the series (12) in (16) can be substantially accelerated. In fact, in [37] a method is specified for a) partitioning I_i symmetrically about its midpoint into three subintervals, and b) re-expanding (12) about the center points of the subintervals.

In this way the summation of the series can be appreciably speeded up. Such a scheme is particularly advantageous when, as in our case [see [36] and the discussion on (12)], there is an efficient way of computing the coefficients of the specific Taylor series. For this reason, a) and b) as discussed in [37] have been incorporated in the computational algorithm here.

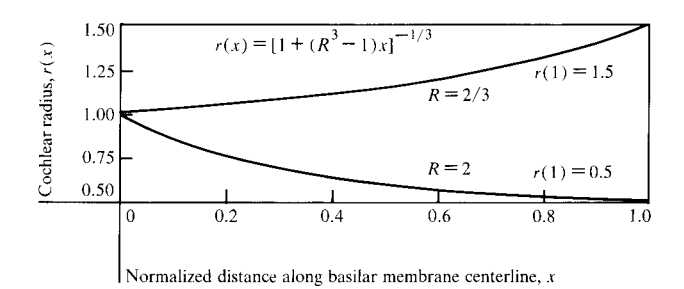


Figure 9 Contracting (R = 2) and expanding (R = 2/3) one-third-power hyperbolic "cochleas" (generators of the surfaces of revolution representing the cochlea).

Computational accuracy check

The constants A and C, in Eq. (2) for the BMC deflection, are determined from the boundary conditions at the helicotrema (x=1). We have chosen three specific supports for the basilar membrane there, with three different expressions, subscripted by h, f and E, for the constants A and C [see formulae after Eq. (4)]. Since the constants are given in terms of $a_{0_p}^{(i)}(1)$, i=0,1,2,3, estimating the errors in A and C—due to an error in $a_{0_p}(1)$ —is very difficult. Analyzing the conditioning of the coefficients matrix in the equations for A and C (for the three different supports at x=1) is not very helpful in obtaining error bounds for A and C.

A way out of this impasse is offered by recalling that for some hyperbolic cochlear shapes [Eq. (7)], the BMC deflection $a_0(x)$ is available in closed form. In particular, for

$$r(x) = \frac{1}{\left[1 + (R^3 - 1)x\right]^{\frac{1}{3}}}, \qquad R = \frac{r(0)}{r(1)},$$
 (23)

we find

$$p_0(x) = 1 - F_1 x - F_2 x^2, (24)$$

and

$$a_{0p}(x) = \frac{2}{D} \left[\frac{x^4}{(m^2 - 4)(m^2 - 16)} - \frac{F_1 x^5}{(m^2 - 9)(m^2 - 25)} - \frac{F_2 x^6}{(m^2 - 16)(m^2 - 36)} \right],$$
 (25)

where

$$F_1 = \frac{1 - P}{1 + (R^3 - 1)/2}$$
 and

$$F_2 = \frac{(1-P)(R^3-1)}{2+(R^3-1)}.$$

From (25) and the formulae for A and C, the deflection of $a_0(x)$ is obtained. For any R, we can describe (i.e., "fit"), to within a specified error, the corresponding hyperbola by a spline. The load and deflection can sub-

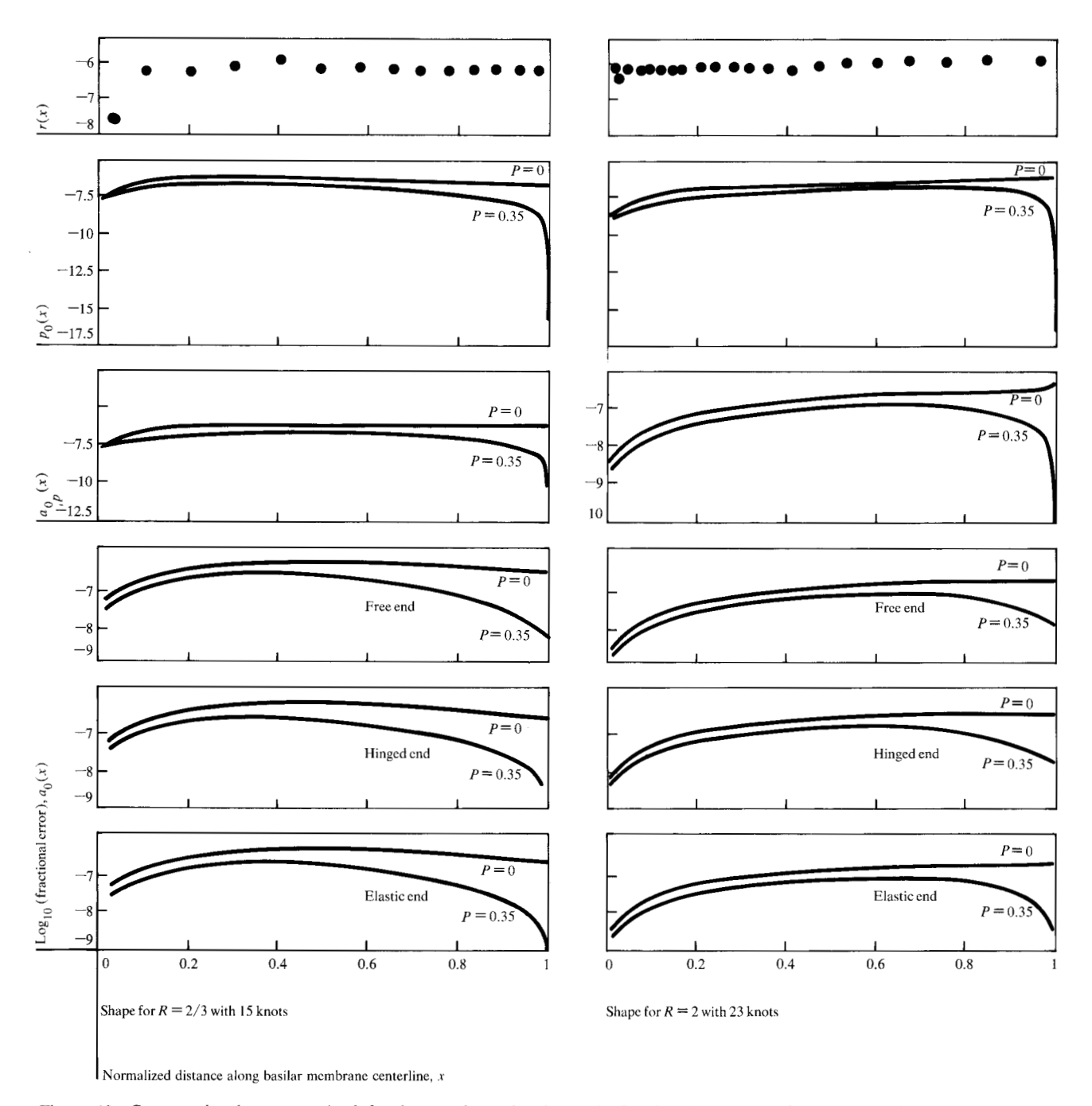


Figure 10 Computational accuracy check for the two shapes in Fig. 9. The fractional error for r(x) is computed halfway between the knots where the deviation between the spline and the exact shape is maximum. The shape for R = 2/3 required 15 and that for R = 2 required 23 knots to yield the accuracy shown in r(x). Additionally at x = 0 and x = 1, the hyperbola's exact slope was imposed on the spline.

sequently be computed from the truncated series in (13) and (15) and can be compared to the exact values obtained from (24) and (25). Such a comparison reveals whether A and C are computed accurately, and in fact provides an overall check for the accuracy of the algorithm. Below, we show such a comparison for two exact

shapes (Fig. 9) obtained from Eq. (23). One is contracting with R=2 and the other expanding with R=2/3. Note that the cochlear radius r(x) is normalized with r(0)=1. For consistency with our previous error estimates we use as our comparison criterion for a variable V(x), the fractional (relative) error defined by

$$F \cdot E[V(x)] = \left| \frac{V_{\rm E}(x) - V_{\rm C}(x)}{V_{\rm E}(x)} \right|,$$

where the subscript E indicates the exact values obtained from (23) through (25), and C indicates the value obtained from (13) and/or (15) for the hyperbolic shape approximated by a spline.

The results of the comparison are summarized in Fig. 10. In order to obtain $F \cdot E[r(x)] < 10^{-6}$, 15 knots were needed to describe the shape defined by R = 2/3 and 23 knots for the shape given by R = 2. In addition, the slopes for the spline at x = 0 and x = 1 were matched, using the spline interpolation algorithm, to those of the exact shapes obtained from (23). For $\varepsilon = 10^{-5}$ [see (16)], only two terms in the series for $1/r^3(x)$ sufficed on each interval between knots! In both cases and for all the variables, $F \cdot E \le 10^{-6.5}$. As expected from the discussion in the previous section on error bounds, the error is somewhat smaller for $P \ne 0$ (in this case P = 0.35) than for P = 0.

The results in these examples are representative of several comparisons that were actually carried out. They show that the error bounds in (18), (20) and (22) are quite conservative and that the algorithm described above is accurate and reliable. Incidentally, note that the error values in these examples not only bound the propagation of the truncation error in (16) but also the error due to the approximate representation of r(x), obtained from (23), by a spline.

Implementation

The algorithm is implemented on an APL conversational terminal system attached to a graphics display console (described in [38]) — a mode well suited for experimentation with the model. We wish, by means of some examples, to demonstrate the salient features of the system and model.

At first, in order to understand the effects of cochlear taper, defined by R = r(0)/r(1), we examine the three conical shapes shown in Fig. 11. (In all cases we have set N = 0.25. Varying the Poisson ratio does not alter x_{M0} appreciably.) Incidentally, these "cochleas" can be easily generated by means of our spline interpolation, which can produce straight line segments on specified intervals. For shape C, the taper is about 3.33, as in the human cochlea. The load induced by the conical twochambered (i.e., P = 0) cochlear shape increases pointwise with increasing taper. Hence, in the resulting deformation of the basilar membrane centerline, the position x_{M0} of the maximum increases with increasing taper. Recall that it is the position rather than the amplitude of the maximum deflection which, according to the place principle, is characteristic of the input frequency ω . Here the computations are for $\omega \to 0$, so x_{M0} should be

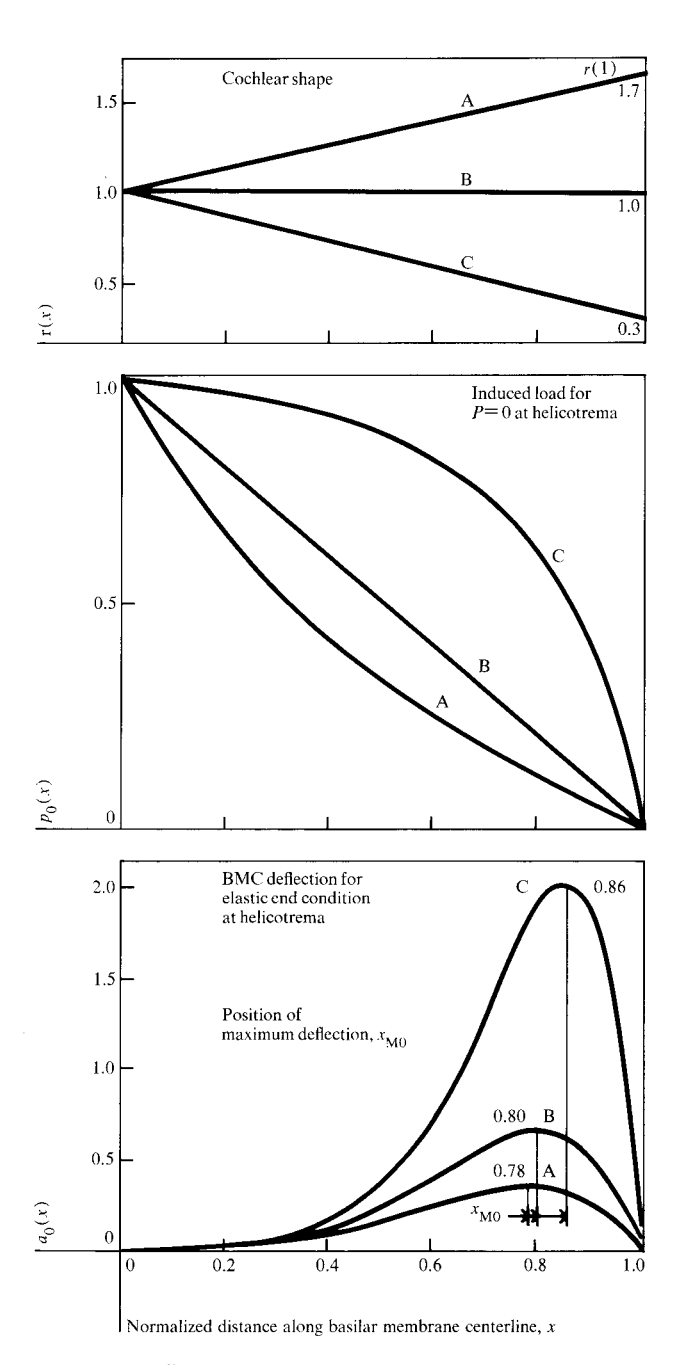


Figure 11 Effect of cochlear taper $-x_{M0}$ increases as the taper R = r(0)/r(1) increases.

as close to the helicotrema at x=1 as possible [see Fig. 7, Eq. (6), and previous discussion]. We can conclude, at least for conical shapes, that a contracting (R>1) cochlea is more desirable, in the sense that it yields a larger $x_{\rm M0}$, than a cylindrical or expanding cochlea. This may be a reason why the human cochlea is contracting. By the way, for hyperbolic cochleas when p is large (see Fig. 8), a comparable variation in the taper produces a more dramatic variation in $x_{\rm M0}$ than for conical cochleas.

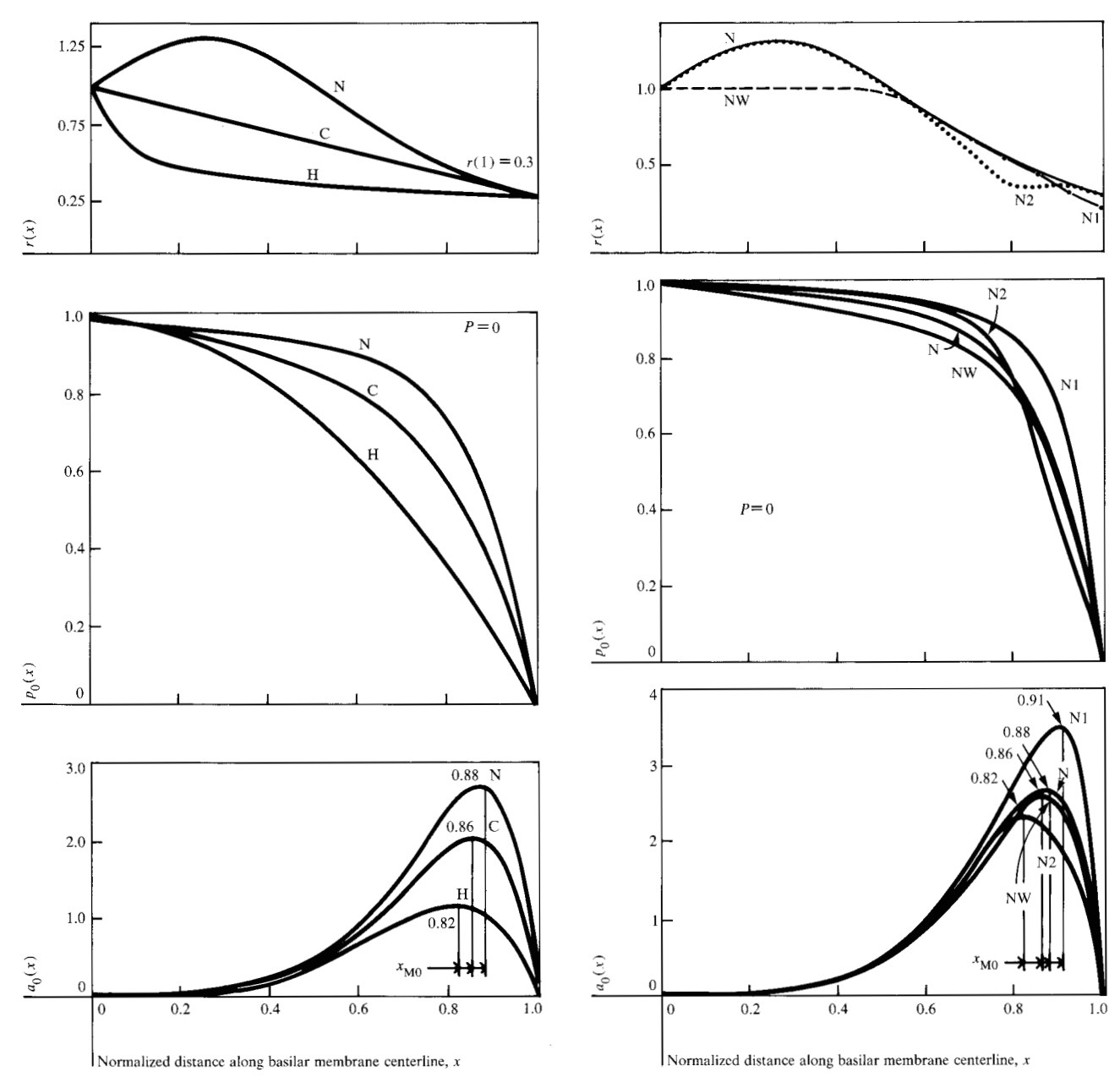


Figure 12 Contracting cochleas. Shape C (also shown in Fig. 11) is given by r(x) = 1 - 0.7x. Shape H is a one-third-power hyperbola for R = 3.33 and N resembles somewhat the shape of the human cochlea.

Figure 13 Effect of pinches and bulges on the basic shape N (also shown in Fig. 12). Shape NW is obtained from N by flattening the bulge. Shape N2 is shape N with a 30 percent pinch at x = 0.8, and shape N1 is N with a 30 percent pinch at x = 1.

On an IBM System VM 370 Model 145 computer, about three seconds of virtual CPU time was required to compute the load and deflection for each cochlear shape shown. In time-sharing mode, the keyboard time was two to three minutes for each shape, including the plots, when the system had a normal number of users. These times are nominal and do not vary much for different cochlear shapes.

Having decided on the desirability of the contracting cochleas we compare next two different shapes having R=3.33, as shown in Fig. 12, with the contracting conical cochlea C. Shape H is a one-third-power hyperbola determined from (23). Shape N resembles the human cochlea, which has a bulge close to the basal end and then narrows down. The results imply that N is superior since it yields the largest x_{M0} . The shape N, however, is

not entirely optimal. For example, a similar shape, not shown, with the bulge shifted toward the apex [having maximum radius r(0.45) = 1.3] yields $x_{M0} = 0.92$.

The cochlear geometry determines x_{M0} in a very complicated way. For P=0, it was empirically found that x_{M0} is approximately determined by the slope $p_0'(1)$ divided by the integral of the load from x=0.5 to x=1.

The algorithm converges slowly when the slope of the cochlear shape is steep. Convergence is accelerated in such cases by partitioning the intervals between the knots specifying the cochlear shape. Subsequently the spline is reconstructed, but with a greater number of knots due to the partitioning. With the cubic portions defined on smaller subintervals the convergence is faster. Furthermore, the partition invariance property of our spline (see [35]) guarantees that the new spline constructed with the larger number of knots yields the same shape.

Earlier we had suggested that there may be clinical reasons for wanting to study perturbations in a particular cochlear shape (see Table 1). This can certainly be done by specifying a sufficient number of knots. However, it is more convenient to have special functions for rapid shape alterations. For this reason we have included functions which generate "pinches" or "bulges" in a given cochlear shape. The user specifies the location where the pinch or bulge is to be centered and the relative amount [in percentage of r(x)] of change desired. Subsequently, in the given cochlear shape, a pinch or bulge normally distributed [again in percentage of r(x)], about the specified point is generated. This is demonstrated in Fig. 13, where the effects of such changes on the shape N are illustrated. When the bulge is leveled, x_{M0} is somewhat reduced. With a pinch at x = 0.8 – just before x_{M0} for N – both x_{M0} and the maximum amplitude are reduced, while a pinch at x = 1 (i.e., past x_{M0} in N) has the opposite effect.

It is evidently very difficult to predict the outcome of various shape modifications. Let us exemplify this further. We chose the simplest shape, cylindrical cochlea, in order to study the consequences of shifting the same pinch to different locations as shown in Fig. 14. Observe that a pinch before x_{M0} reduces x_{M0} and the maximum amplitude, a pinch at x_{M0} slightly reduces x_{M0} and increases the amplitude, while a pinch after x_{M0} increases x_{M0} and the amplitude. In general, contracting the cochlea increases the load while expanding the cochlea results in a reduced load. Pinches (bulges) before x = 0.5 do not alter x_{M0} much but decrease (increase) maximum amplitude. Near x_{M0} , local alterations of the cochlear shape produce significant changes, with bulges producing effects opposite to those produced by pinches. The apical end (x = 1) is the position most sensitive to shape modifications.

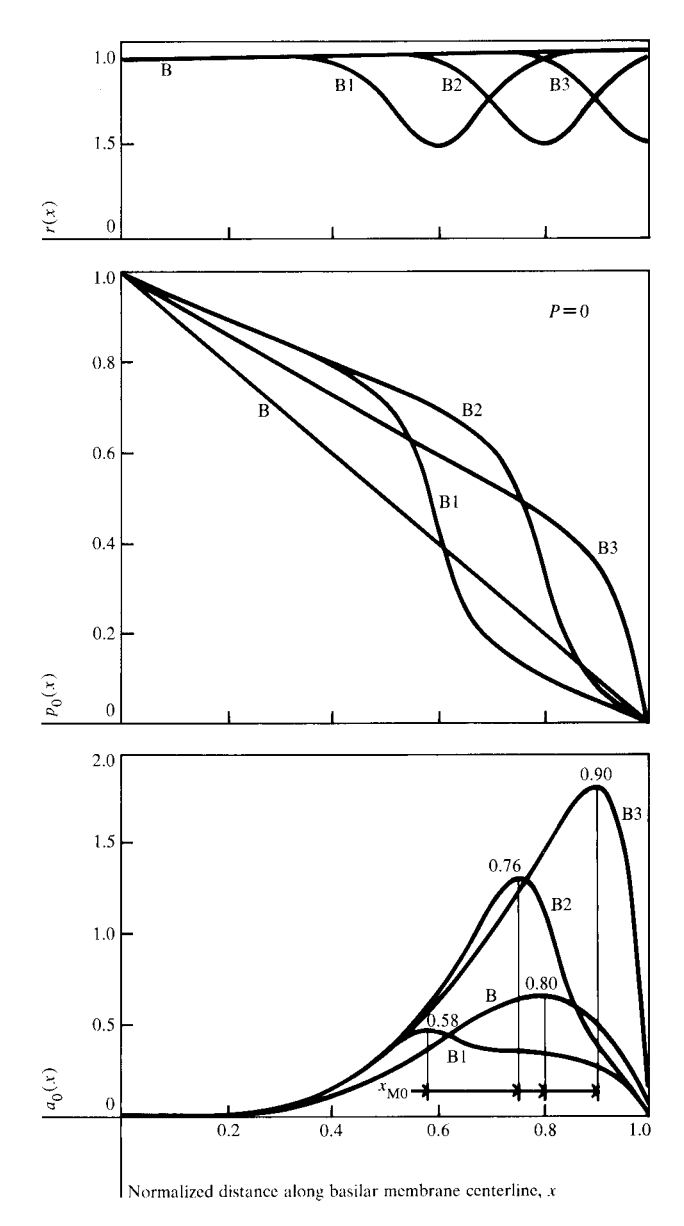


Figure 14 Varying the location of a pinch. Shapes B1, B2 and B3 are obtained from the cylindrical cochlea B by locating a 50 percent pinch at x = 0.6, 0.8, and 1, respectively.

In two-chambered cochleas, as in all our examples so far, P=0, yielding x_{M0} somewhat far from x=1. The real cochlea, however, is three-chambered, with P, the net pressure across the basilar membrane at x=1, being nonzero; ergo the provision for quasi-three-chambered cochlear models having $P\neq 0$ in Eq. (1). In quasi-three-chambered cochleas, x_{M0} is close to the helicotrema (see section on Model) not only for hyperbolic cochleas, as shown in Fig. 8, but also, as we show next, for more general shapes. For the shape BH (Fig. 15), which resembles a hyperbola with a bulge, there is a dramatic change from $x_{\text{M0}}\approx 0.82$ when P=0, to $x_{\text{M0}}\approx$

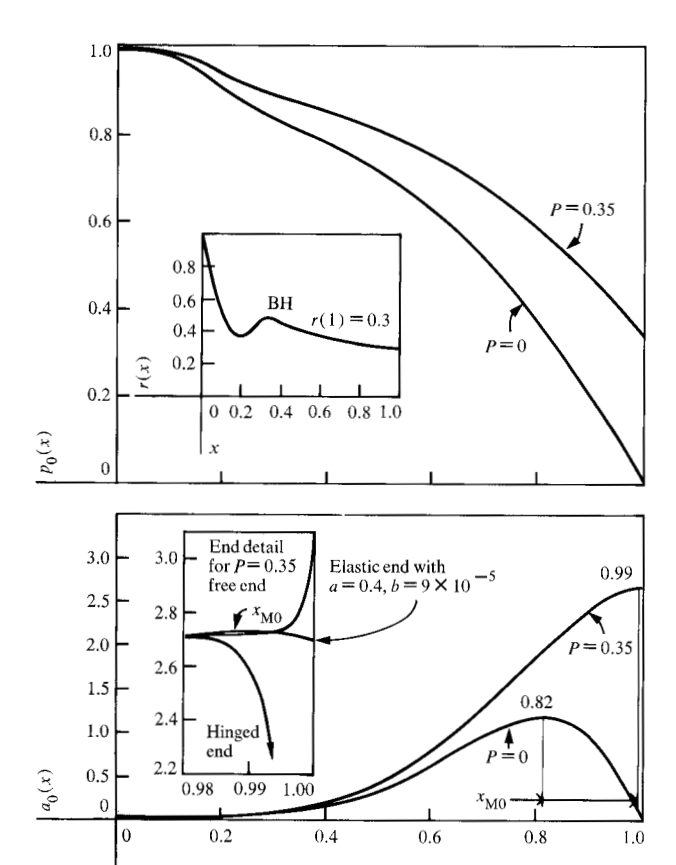


Figure 15 Two-chambered (P=0) and quasi-three-chambered cochlea with the same shape BH. Notice, in end detail of the deformation, the flapping of the free end.

Normalized distance along basilar membrane centerline, x

0.99 when P = 0.35. As long as x_{M0} is far from the helicotrema, it is not influenced by the end support there. Now, as the end detail (for $0.98 \le x \le 1.00$) of the deformation vividly portrays, the matter of proper boundary conditions at x = 1 can no longer be ignored. A glance at Fig. 7 shows that because the basilar membrane moves at x = 1, this endpoint cannot be fixed. This rules out the hinged-end boundary condition. Allowing the basilar membrane to be unconstrained at x = 1, corresponding to the free-end condition, poses a problem. In the last half percent or so of its length the basilar membrane seems to flap (recall that the envelope of the oscillation is symmetrical about the x axis and only the positive $a_0(x)$ portion is shown). Such a spirited oscillation could tear the membrane. This does not occur with the elasticend condition at x = 1. The implication is that the microstructure of the basilar membrane at its apical end is approximated by the support that a thin beam at x = 1would provide. Intrigued by this prospect, Dr. F. Linthicum of the Ear Research Institute in Los Angeles provided a preliminary confirmation of this after examining human cochleas with a scanning electron microscope [39]. He found that the basilar membrane becomes noticeably more fibrous very close to the helicotrema, with a rather strong "ligament" constraining its motion there to prevent it from flapping and tearing. The flexural and torsional strengths of this ligament are measured by the constants a and b [defined just prior to A_E and C_E below Eq. (4)]. With the elastic-end condition, then, we obtain $x_{M0} = 0.99$ for the shape BH in Fig. 15 without any flapping of the basilar membrane.

The effect of increasing P from 0 to 0.36 in three contracting cochleas is seen in Fig. 16. While N is a "better" shape (i.e., x_{M0} larger) than BH when the cochlea is two-chambered, the reverse is true for quasi-threechambered cochleas. In fact, the shape BH satisfies condition (6) with $x_{M0} = 1$. Actually, BH is a more realistic representation of the human cochlea than N. Though the cochlea bulges initially, the stapes, where the input occurs, is positioned after the peak in the bulge. This corresponds to the initial portion of BH (or a curve such as H) where r(x) is monotone decreasing. The bulge in BH is an attempt to represent some of the local variations-from strictly monotone decreasing-in cross-sectional areas of the actual cochlea. The difference in performance (i.e., difference in x_{M0}) between N and BH (or H) suggests that the position of the stapes on the bulge is fairly significant.

In Fig. 17 we show a comparison for shapes N and BH with BH1 obtained by putting a bulge close to the apical end in H. The variation in $x_{\rm M0}$ for BH1 as P increases from 0 to 0.36 is rather striking. Among other things the comparison suggests that BH is "close" to an "ideal" shape in the sense of yielding $x_{\rm M0} = 1$.

These examples illustrate the difficulty of describing the dependence of $x_{\rm M0}$ on cochlear geometry. Hopefully, they also illustrate the kind of information that can be gained through interactive experimentation with the model.

Acknowledgments

In the course of this work the author benefitted from collaboration with the Ear Research Institute of Los Angeles. He especially thanks Dr. Fred Linthicum of this Institute for numerous valuable discussions and for sharing his experience and data.

The author is grateful to Paul Neiswander, of the IBM Los Angeles Scientific Center, for expertly writing the APL program, carrying out the computations, and making numerous suggestions and contributions, and to Vicky Jones for the beautiful drawings in Figs. 4 and 5.

The user experience gained, while the program was being developed, from the Harvey Mudd College group [40] is appreciated.

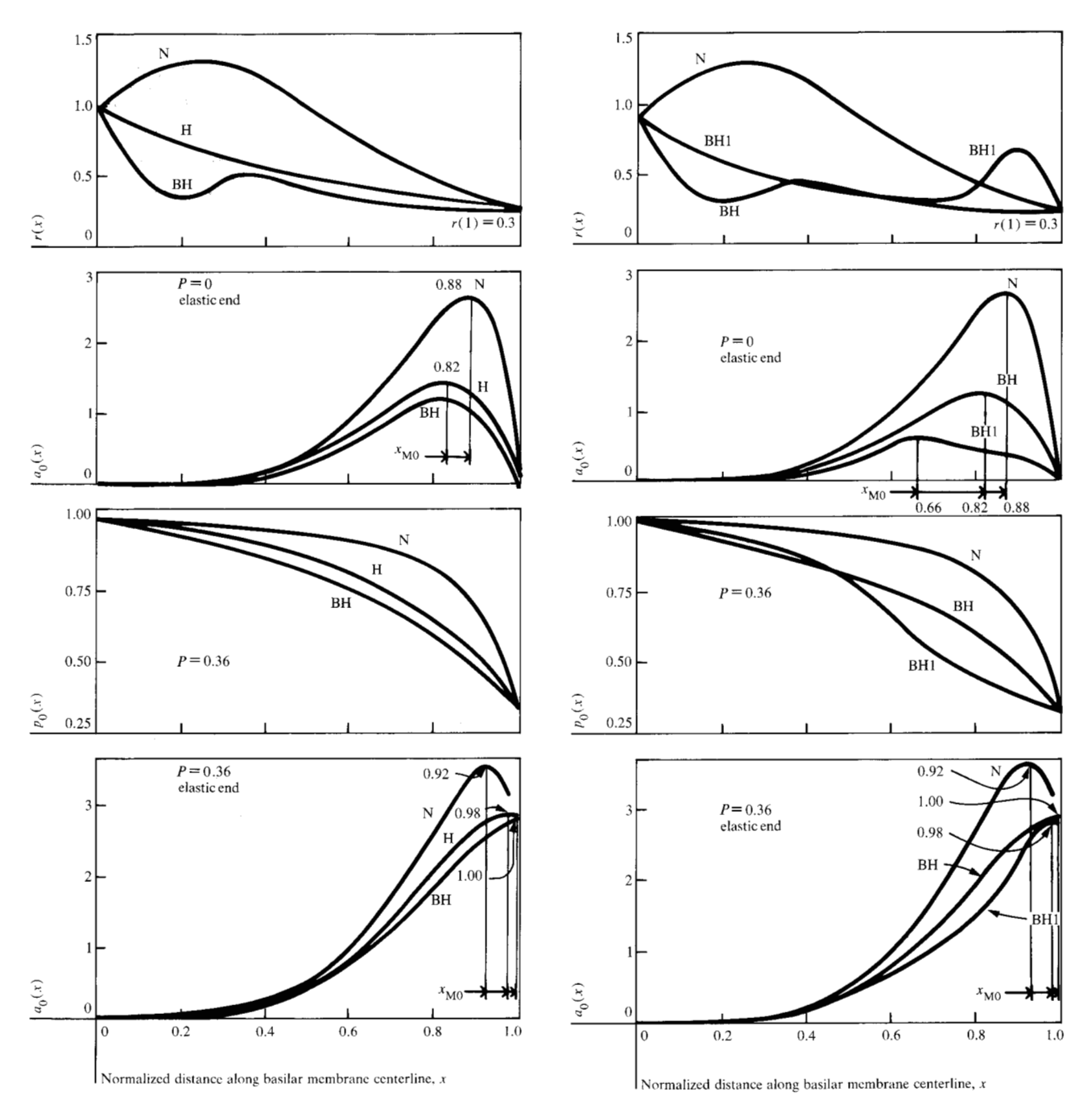


Figure 16 Comparison of three contracting shapes for twochambered and quasi-three-chambered cochleas. Of the three, BH most closely resembles the actual cochlea.

Figure 17 Three cochlear shapes indicating the effects of local variations in geometry for two-chambered and quasi-three-chambered cochleas.

The interactive graphics program described here has been classified by the IBM Corporation as a Research Experimental Program and is freely available for research.

References and notes

 E. G. Wever and M. Lawrence, *Physiological Acoustics*, Princeton University Press, Princeton, NJ, 1954.

- 2. T. S. Littler, *The Physics of the Ear*, The MacMillan Co., New York, 1965.
- 3. H. Davis, "Excitation of Auditory Receptors," *Handbook of Physiology, Section 1 (Neurophysiology)*, Vol. 1, J. Field, ed., Amer. Physiol. Soc., Washington, DC, 1959, p. 565.
- H. L. F. von Helmhotz, Sensations of Tone, Dover Publications, New York, 1954. (Republication of the second (1885) edition of the Ellis translation of Die Lehre von den Tonempfindungen, originally published by Longmans & Co., London, in 1859.)

- L. C. Peterson and B. P. Bogert, "A Dynamical Theory of the Cochlea," J. Acoust. Soc. Amer. 22, 369 (1950).
- the Cochlea," J. Acoust. Soc. Amer. 22, 369 (1950).
 O. F. Ranke, "Theory of Operation of the Cochlea: A Contribution to the Hydrodynamics of the Cochlea," J. Acoust. Soc. Amer. 22, 772 (1950).
- 7. H. Fletcher, "On the Dynamics of the Cochlea," J. Acoust. Soc. Amer. 23, 637 (1951).
- 8. J. Zwislocki, "Review of Recent Mathematical Theories of Cochlear Dynamics," J. Acoust. Soc. Amer. 25, 743 (1953).
- 9. A. Inselberg and H. von Foerster, "A Mathematical Model of the Basilar Membrane," J. Math. Biosc. 7, 341 (1970).
- M. Lieberstein, "The Basilar Membrane as a Uniformly Loaded Plate Clamped on Two Spiral Boundaries in a Plane or on Two Helical-spiral Boundaries," J. Math. Biosc. 12, 281 (1971).
- 11. M. Lesser and D. Berkley, "Fluid Mechanics of the Cochlea. Part 1," J. Fluid Mech. 51, 497 (1972).
- 12. C. Steele, "Behavior of the Basilar Membrane with Puretone Excitation," J. Acoust. Soc. Amer. 55, 148 (1974).
- 13. M. Viergever and J. Kalker, "On the Adequacy of the Peterson-Bogert Model and on the Effects of Viscosity in Cochlear Dynamics," J. Eng. Math. 8, 149 (1974).
- P. Allaire, S. Raynor, and M. Billone, "Cochlear Partition Stiffness – a Composite Beam Model," J. Acoust. Soc. Amer. 55, 1252 (1974).
- 15. W. Siebert, "Ranke Revisited—A Simple Short-wave Cochlear Model," J. Acoust. Soc. Amer. 56, 599 (1974).
- 16. S. M. Novoselova, "The Basilar Membrane as an Elastic Plate," Sov. Phys. Acoust. 21, 56 (1975).
- G. Zweig, R. Lipes, and J. Pierce, "The Cochlear Compromise," J. Acoust. Soc. Amer. 59, 975 (1976).
- J. van Dijk, "On the Hydrodynamics of the Inner Ear, Theoretical Part. A Mathematical Model," Acustica 35, 190 (1976).
- A. Inselberg and R. Chadwick, "Mathematical Model of the Cochlea, I: Formulation and Solution," SIAM J. Appl. Math. 30, 149 (1976).
- R. Chadwick, A. Inselberg, and K. Johnson, "Mathematical Model of the Cochlea, II: Results and Conclusions," SIAM J. Appl. Math. 30, 164 (1976).
- A. Inselberg, "Quasi-Three-Chambered Model of the Cochlea," to be submitted for publication.
- 22. A. Inselberg, "Cochlear Dynamics: The Evolution of a Mathematical Model," SIAM Rev., to be published.
- 23. M. R. Schroedder, "Models of Hearing," *Proc. IEEE* 63, 1332 (1975).
- G. von Békésy, Experiments in Hearing, McGraw-Hill Book Co., Inc., New York, 1960. Figure 7 used by permission.
- B. Johnstone and A. Boyle, "Basilar Membrane Vibration Examined With the Mössbauer Technique," Science 158, 389 (1967).
- W. Rhode, "Observations of the Vibration of the Basilar Membrane in Squirrel Monkeys Using the Mössbauer Technique," J. Acoust. Soc. Amer. 49, 1218 (1971).
- 27. L. Kohllöffel, "A Study of Basilar Membrane Vibrations, I, II, III," Acustica 27, 49 (1972).
- C. R. Steele, A Possibility for Sub-Tectorial Membrane Fluid Motion, Basic Mechanisms of Hearing, A. R. Møller, ed., Academic Press, New York, 1973, p. 69.

- 29. W. H. Huggins and J. C. R. Licklider, "Place Mechanisms of Auditory Frequency Analysis," *J. Acoust. Soc. Amer.* 23, 290 (1951).
- A. Inselberg and H. von Foerster, "Linear Property Filters," #41 in Collected Works of the Biological Computer Laboratory, University of Illinois, K. L. Wilson, ed., Illinois Blueprint Co., Peoria, 1976.
- E. G. Wever, Theory of Hearing, John Wiley & Sons Inc., New York, 1949.
- 32. R. S. Chadwick, M. Israeli, and U. Levite, "Virtual Mass and Damping Corrections to a One Dimensional Formulation of Cochlear Mechanics with an Application to a Three Chamber Model," *Israel J. Tech.* 13, 168 (1975).
- I. Friedman, Pathology of the Ear, Blackwell Scientific Publications, Oxford, 1974.
- B. Dimsdale, "On Multiconic Surfaces," Technical Report G320.2661, IBM Scientific Center, Los Angeles, CA, 1974
- 35. A. Inselberg, "Cubic Splines with Infinite Derivatives at Some Knots," *IBM J. Res. Develop.* 20, 430 (1976).
 36. A. Inselberg, "The Determinant of a Class of Toeplitz-
- 36. A. Inselberg, "The Determinant of a Class of Toeplitz-Hessenberg Matrices Arising in Power Series," *J. Math. Anal. Applic.*, to be published.
- 37. A. Inselberg, "Accelerating the Convergence of Taylor Series," to be submitted for publication.
- 38. GRAPHPAK, No. SB21-0412-0, IBM Corporation, Data Processing Division, White Plains, NY, 1972.
- 39. Progress Report 1974, Ear Research Institute, Los Angeles, p. 14.
- 40. R. Finley, "Mathematical Treatment of an Inner Ear Disease," (internal journal, Harvey Mudd College, Pomona, CA) Interface 4, 20 (1976). The program described in this paper was used in a study by Harvey Mudd College students led by R. Finley under the supervision of Professor C. Coleman. With data obtained from the Ear Research Institute of Los Angeles, the model was used to determine if some of the hearing loss due to cochlear otosclerosis could be attributed to distortions in the cochlear geometry. It was found that the otosclerotic distortions occur in a portion of the cochlea where the maximum $a_0(x)$ is particularly sensitive to shape variations. To properly investigate cochlear otoscelerosis, however, it was felt that the model must also accommodate variations in the shape of the basilar membrane. In fact, the necessary modifications for doing this have been initiated by this group. The results of this study suggest a surgical procedure for reversing some of the hearing loss due to cochlear otosclerosis.

Received February 28, 1977

The author is located at the IBM Los Angeles Scientific Center, 9045 Lincoln Boulevard, Los Angeles, California 90045.